Comparison of Computational Aeroacoustics Prediction of Acoustic Transmission Through a 3D Stator with Experiment

Ray Hixon*
University of Toledo, Toledo, OH 43606
Edmane Envia†
Milo Dahl‡
Daniel Sutliff§
NASA Glenn Research Center, Cleveland, OH 44135

In this paper, numerical predictions of acoustic transmission through a 3D stator obtained using the NASA BASS code are compared with experimentally measured data. The influence of vane count and stagger as well as frequency and mode order on the transmission loss is investigated. The data-theory comparisons indicate that BASS can predict all the important trends observed in the experimental data.

I. Introduction

Computational Aeroacoustics (CAA) is focused on the simulation of acoustic fields produced by unsteady flows (see Refs. 1-4 for reviews of the progress made and challenges). To achieve this goal, it is necessary to accurately simulate the evolution of flow disturbances, which requires the use of high-accuracy spatial and temporal numerical schemes. As these schemes have been developed and validated, the application problems of interest have also increased in complexity, now typically involving realistic nonlinear flows about complex geometries.

An application of interest to the aircraft industry is the prediction of acoustic transmission through turbomachinery blade rows. In the past, analytical theories for unloaded flat plate configurations were developed (e.g., Ref. 5), but these do not account for the effect of realistic geometry, loading, and non-uniform mean flows. Numerical methods have also been developed for infinitely thin flat plates,[6] and later work has incorporated actuator disks to represent the effect of blade loading.[7] These theories have been used to validate two-dimensional CAA predictions.[8,9]

As a step towards the ultimate goal of predicting acoustic transmission through realistic fan stages, CAA simulations of acoustic transmission through realistic 3D stator geometries with no mean flow have been performed. This work relies on a new experimental database acquired at NASA Glenn Research Center[10] to serve as a benchmark for assessing the performance of the NASA BASS CAA code. The results highlight the ability of CAA to accurately predict acoustic propagation, transmission, reflection, and scattering from 3D stator vanes. The cases shown provide verification of the capability of the BASS code to accurately predict the effect of varying stator geometries on a range of incident acoustic modes and identify the challenges that remain.

*Associate Professor, Mechanical, Industrial, and Manufacturing Engineering (MIME) Department, Senior Member AIAA.
†Research Aerospace Engineer, Acoustics Branch, Associate Fellow AIAA.
‡Senior Research Scientist, Acoustics Branch, Senior Member AIAA.
§Aerospace Engineer, Acoustics Branch, Associate Fellow AIAA.

II. Numerical Solution of the Governing Equations

The BASS code is an unsteady CAA code, which uses explicit fourth-order time marching schemes combined with high order spatial differencing schemes to accurately solve the unsteady nonlinear Euler equations.[11–16]

The BASS code solves the nonlinear Euler or Navier-Stokes equations in chain-rule curvilinear form, using a finite-difference time-domain approach. For topological flexibility, the BASS code uses structured multiblock grids. For portability and maintainability, BASS is written in standard Fortran 2003, and is parallelized using the MPI-1[17] standard. BASS has been tested on a range of compilers and MPI implementations, and has been validated on a number of benchmark aeroacoustics problems.

The BASS code has a number of spatial differencing schemes, artificial dissipation methods, and explicit time marching schemes implemented. For this work, the BASS code was run using the HALE-RK67 time marching scheme.[18] An automatic shock-capturing dissipation model[19] was used, based on the explicit filters of Kennedy and Carpenter.[20] The Tam and Webb 7-point optimized fourth-order DRP scheme was used for the spatial differencing.[21] The nonreflecting boundary conditions of Giles[23] were used at the driver and far-field boundaries, combined with a source term used to impose acoustic modes at the driver boundary.

III. Description of Experimental Test Cases

Recently, an experimental stator transmission database has been obtained at the NASA Glenn Research Center.[10] The database was acquired on the Advanced Noise Control Fan[24,25] (ANCF) test bed that was built in the early 1990s[26,27] to evaluate noise reduction concepts and to provide databases for CAA code validation. Figure 1 shows the Aero-Acoustic Propulsion Laboratory where the ANCF is located and a photo of the ANCF. Only a subset of the database will be described here.

A Configurable Fan Artificial Noise System[10] (CFANS) was utilized to generate and control circumferential modes (m) and radial modes (n) in the absence of a mean flow. The modes were measured by the Rotating Rake mode measurement system,[28] which was developed at the NASA Glenn Research Center in the 1990s to measure turbofan duct acoustic modes. The system is a continuously rotating radial microphone rake that is inserted into the inlet of the duct. It provides a complete map of the acoustic duct modes present in a ducted fan. The baseline case was a clean duct, with no stator vanes or fan blades. A parametric set of modes was generated at the aft driver set, and measured by the rotating rake at the inlet. Fourteen stator vanes at a 45^o stagger angle or twenty-eight stator vanes at a 20^o stagger angle were installed and the rotating rake mode measurements were repeated. It is assumed that the source does not change in the presence of the stators, so that the acoustic transmission can be computed by subtracting the mode PWL measured with stators installed from the mode PWL measured in the clean configuration. Table 1 provides the modes generated and their cut-off ratio at the measurement location inside the duct, for the studies documented in this paper. The experimental setup is illustrated in Figure 2.

In the experimental data, there are two primary sources of error. The first source of error is the error in the physical measurement, which is within ± 1 dB. The second source of error is modeling error, which arises from the postprocessing algorithms used to determine the power level of the acoustic modes from the measured data. One source of modeling error arises from the presence of acoustic modes propagating in both the positive and negative axial direction in the duct.[32] These modes cause modeling error because the single row of microphones used in the rotating rake cannot distinguish between the contribution of each of the two families of modes; thus, the postprocessed sound power level for a given azimuthal mode is an unknown combination of the modes propagating in each direction.

IV. Computational Details

As shown in Figure 3, the computational domain has a far-field boundary outside the ANCF inlet, continues into the duct and has another boundary at the acoustic driver location inside the duct. The incoming acoustic modes are imposed at this boundary. The analytical development of the imposed acoustic modes is given in Appendix I. The Giles[23] nonreflecting boundary condition is used to allow outgoing waves to exit the computational domain with minimal reflection.

For all cases, a reference grid is generated using the GridPro/az3000 grid generator.[29] In this reference grid, the stators have zero stagger angle for ease of topology definition and grid generation. The grids have a

Figure 1. Experimental Facilities at NASA Glenn Research Center: (a) Aero-Acoustic Propulsion Laboratory; (b) Advanced Noise Control Fan.

Table 1. Experimental Measurements at Inlet

Case	Mode (m,n)	Frequency	Cutoff Ratio At Inlet	Cutoff Ratio At Driver	Clean PWL (dB)	14 Vane PWL (dB)	28 Vane PWL (dB)
1	$(-2,0)$	480 Hz	1.77	2.01	111.1	111.3	110.7
2	$(+2,0)$	480 Hz	1.77	2.01	111.1	111.3	110.7
3	$(-6,0)$	960 Hz	1.44	1.45	106.6	103.6	106.2
4	$(+6,0)$	960 Hz	1.44	1.45	106.2	105.8	105.5
5	$(-4,0)$	480 Hz	1.02	1.04	113.0	108.1	103.3
6	$(+4,0)$	480 Hz	1.02	1.04	113.5	108.4	103.7

minimum of 10 grid points per wavelength of the highest-frequency acoustic modes, which is well within the resolution capabilities of the DRP scheme. Once the reference grid has been obtained, the AFRL GridWarp volume grid deformation tool of Melville[30] was used to rotate the stators to the desired stagger angle.

V. Results and Discussion

The BASS code was run for the full set of frequencies and modal inputs for the baseline, 14 vane, and 28 vane configurations. For each case, a single azimuthal and radial mode was imposed at the driver location, with a reference mode pressure amplitude of 1.4 Pa.

During the computational run, the flow was converged to a periodic state and solution data was saved for the final two cycles of the disturbance mode after convergence. This data was then postprocessed using temporal and azimuthal Fast Fourier transforms to obtain the radial distribution of the pressure and axial velocity perturbations in the duct. A least-squares method was then used to find the amplitudes of all cut-on modes, from which the mode power level is calculated.

A. Evaluation of the Numerical Solution Accuracy

In the numerical simulations of acoustic transmission, there are a number of possible sources of error. Two major sources of error are due to the imposition of the input acoustic modes and spurious reflections of outgoing acoustic modes at the driver location.

For each simulation, the power level of the imposed acoustic mode was checked at a number of axial locations in the vicinity of the driver. Even in the cases for which the modes were near cutoff, the power

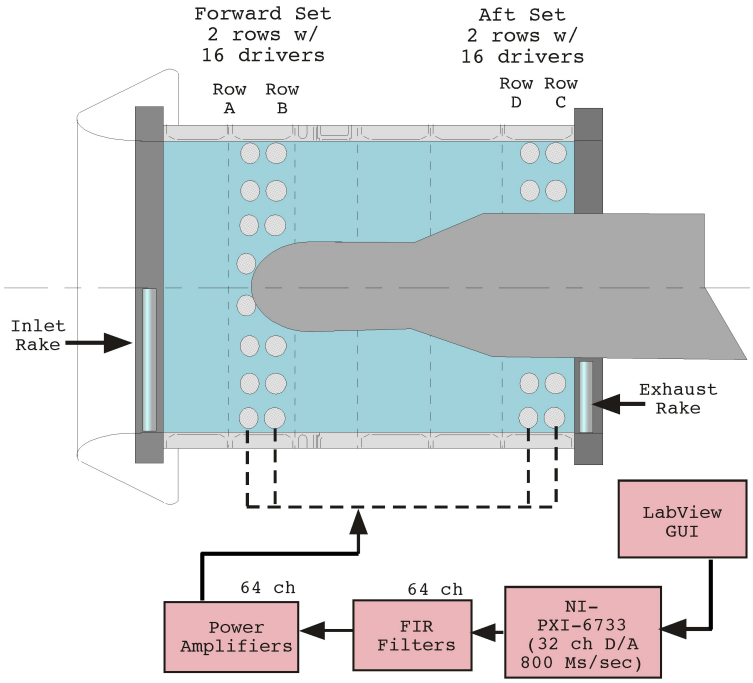

Figure 2. Schematic of the experimental setup for the ANCF stator transmission tests (exhaust rake was not used in these tests).

level of the imposed mode was accurate to within ±1 dB. For the cases with well cut-on modes, the power level of the imposed mode(s) was accurate to within ±0.3 dB.

The errors in the imposed acoustic modes have two sources. First, the actual mode specification may be numerically inconsistent, causing the computed mode to have an incorrect phase and/or amplitude. Secondly, if there is an outgoing mode at the driver location, a spurious reflection may occur due to the boundary conditions; this reflection will modify the amplitude and phase of the imposed mode.

In order to determine the relative importance of these two sources of error, the solutions were postprocessed to determine the levels of the modes propagating in the positive and negative axial directions. The imposed modes propagate in the axial direction towards the inlet ($-x$ direction), while the outgoing modes propagate in the $+x$ direction. These outgoing modes can be generated by the presence of stator vanes, by axial variation in the centerbody geometry, and by the inlet geometry. Investigation showed that the errors due to spurious reflections from the driver location boundary condition caused the majority of errors in the imposed acoustic modes.

Each solution was tested to ensure that the imposed modes were dominant; investigation showed that the solutions had a signal-to-noise ratio of at least 60 dB. In this case, the 'noise' in the numerical prediction is due to truncation error from finite-precision arithmetic.

B. Comparison of Numerical Results to Experimental Data

In the experimental database, the power level of the acoustic modes is given at the inlet plane. The power level of the acoustic modes at the driver location is not given.

In the numerical tests, a mode perturbation pressure amplitude of 1.4 Pa was imposed at the driver plane. Since the flow perturbations are very small for this simulation, the solution is effectively linear and can thus be scaled to compare with the experimental data.

To accomplish this, the numerically predicted power level of the input mode propagating in the $-x$ direction at the inlet measurement location is scaled to match the experimental data for the 'clean' configuration. This gave a numerical prediction for the power level of the input mode at the driver location, which was then used to scale the mode power levels identically for all three configurations. Table 2 gives the numerical predictions for the mode power levels at the driver location.

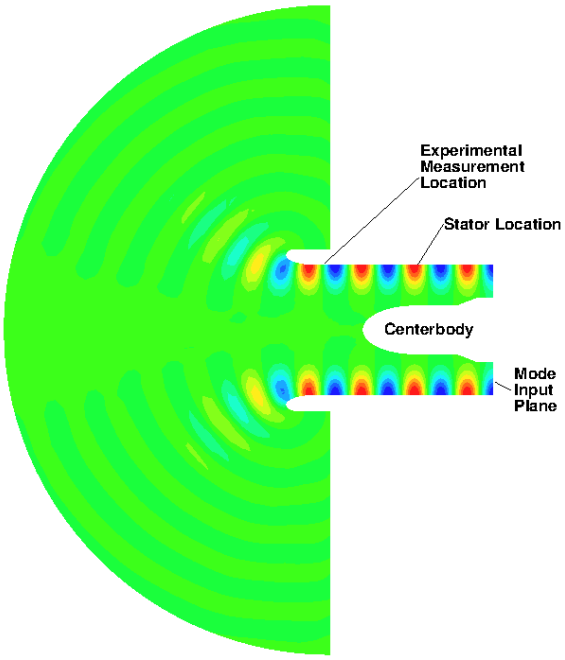

Figure 3. Schematic of the computational domain for the ANCF stator transmission tests.

It is important to note that the experimental mode power level has been used to scale the mode propagating in the $-x$ direction. This inherently assumes that the power level of the mode propagating in the $+x$ direction is small in comparison. The numerical predictions were used to quantify the accuracy of this assumption. Table 2 shows that this is a good assumption except in the case of a nearly cut-off mode (cases 5 and 6).

Finally, in order to obtain a direct comparison for the acoustic transmission losses between the numerical and experimental data, the numerical prediction for the input mode power level at the driver location was used to calculate the actual experimental acoustic transmission losses.

Table 2. Numerical Predictions for Clean Configurations

Case	Mode (m,n)	Frequency	Predicted Driver Location PWL (dB)	Predicted Inlet Reflection PWL (dB)
1	$(-2,0)$	480 Hz	111.1	90.7
2	$(+2,0)$	480 Hz	111.1	90.6
3	$(-6,0)$	960 Hz	106.6	79.1
4	$(+6,0)$	960 Hz	106.2	78.7
5	$(-4,0)$	480 Hz	115.1	108.7
6	$(+4,0)$	480 Hz	115.6	109.2

C. Results for Modes $(\pm 2, 0)$ at 480 Hz

Figure 4 illustrates the propagation of these acoustic modes through the three geometries. The modes have a long wavelength compared to the stator gap and are propagating very nearly in the axial direction. For this reason, both stator geometries are 'open' to the modes, which results in very little acoustic reflection or transmission loss. Reflection loss is defined here as the difference in the mode power level of the incident mode and the reflected mode.

Table 3 compares the numerical predictions for transmission loss with the transmission loss computed

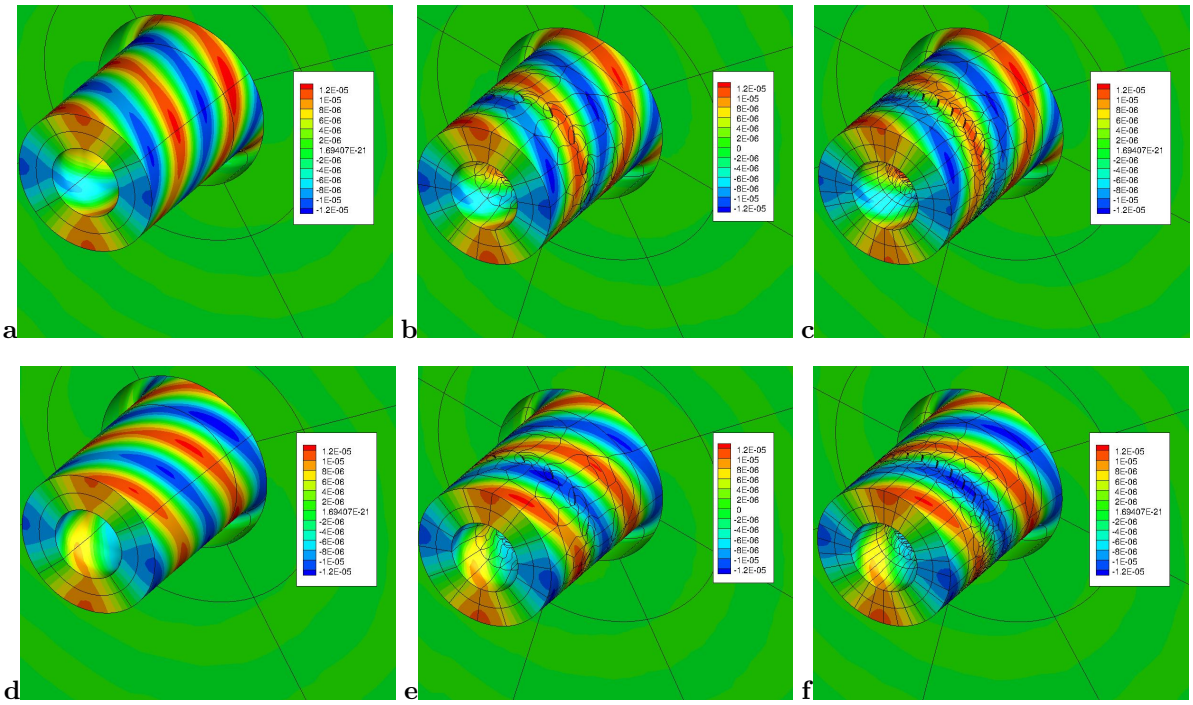

Figure 4. Predicted perturbation pressure contours at the start of a cycle for $(\pm 2, 0)$ mode at 480 Hz through the three ANCF configurations (a: $(-2, 0)$ clean, b: $(-2, 0)$ 14 vanes, c: $(-2, 0)$ 28 vanes d: $(+2, 0)$ clean, e: $(+2, 0)$ 14 vanes, f: $(+2, 0)$ 28 vanes)

from the experimental data. For completeness, the numerically computed reflection loss is also included in the table. Recall from Tables 1 and 2 that the modes reflected from the inlet have a power level 20 dB below that of the incident modes; thus, the measured data should have very low error due to the postprocessing.

As the comparison shows, the predicted acoustic transmission is within the range of experimental error for these test cases.

Table 3. Predicted and Measured Transmission and Reflection Losses (dB) for Modes $(\pm 2, 0)$ at 480 Hz

Case	Mode (m,n)	Transmission Loss 14 Vane (Pred/Exp)	Reflection Loss 14 Vane	Transmission Loss 28 Vane (Pred/Exp)	Reflection Loss 28 Vane
1	$(-2, 0)$	-0.2/+0.2	-17.6	0.0/-0.4	-20.1
2	$(+2, 0)$	-0.2/+0.2	-17.0	0.0/-0.4	-19.8

D. Results for Modes $(\pm 6, 0)$ at 960 Hz

Figure 5 illustrates the propagation of these acoustic modes through the three configurations. As in the previous case, these modes have a long wavelength compared to the stator gap, but are propagating at a large angle to the axial direction. For this reason, the stator geometries are open to the modes rotating in the positive direction and closed to a varying degree to the modes rotating in the negative direction. Thus, the direction of rotation has a large impact on the reflection and transmission losses.

For the 14 vane stator geometry, Tyler and Sofrin theory [33] predicts that predicts that mode energy can scatter from the imposed azimuthal mode 6 to the cut-on counter-rotating azimuthal mode 8. Both the experimental and numerical data show that this scattering is most pronounced for the $(-6, 0)$ mode, but much less energetic for the $(+6, 0)$ mode, as would be expected. In Figure 5 (b), the interference patterns caused by the presence of the counter-rotating mode can be clearly seen.

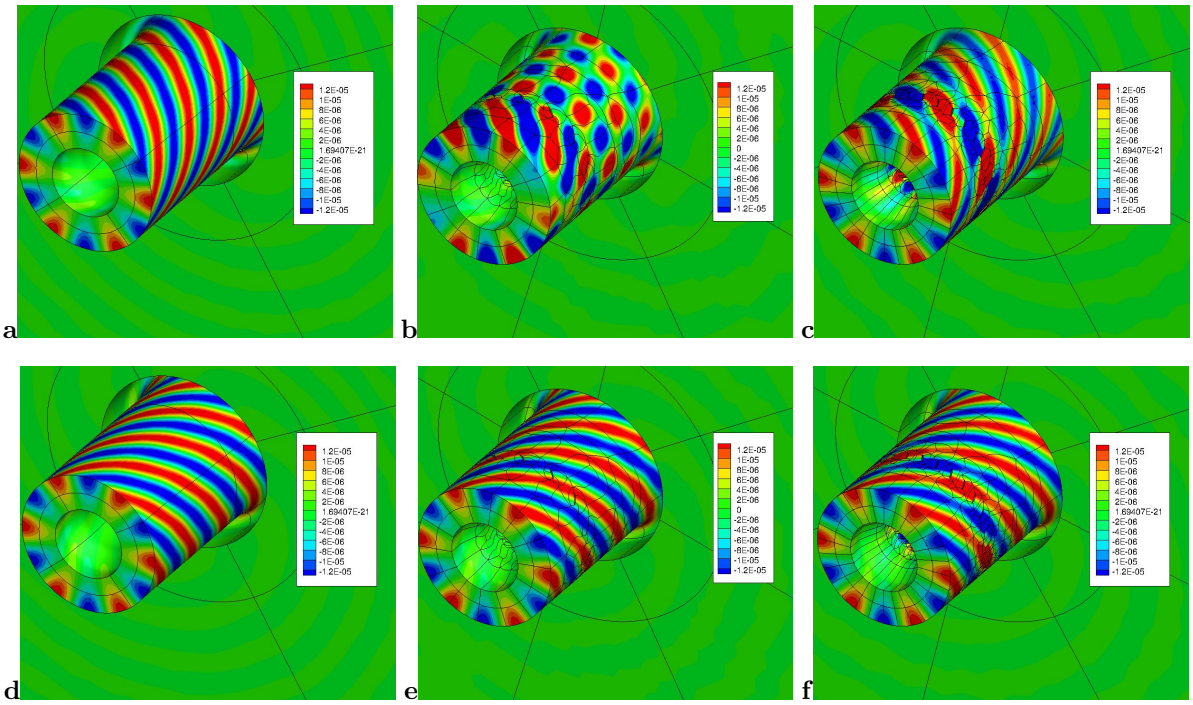

Figure 5. Predicted perturbation pressure contours at the start of a cycle for $(\pm 6, 0)$ **mode at 960 Hz through the three ANCF configurations (a:** $(-6, 0)$ **clean, b:** $(-6, 0)$ **14 vanes, c:** $(-6, 0)$ **28 vanes d:** $(+6, 0)$ **clean, e:** $(+6, 0)$ **14 vanes, f:** $(+6, 0)$ **28 vanes)**

The numerical results for mode $(+8, 0)$ may be contaminated by the presence of strong spurious reflections from the driver location boundary condition. In the numerical data, the mode power level of the scattered $(+8, 0)$ mode, propagating in the $-x$ direction from the stator to the driver location, has a mode power level of 102.8 dB. This strong mode itself reflects (spuriously) from the driver location boundary, propagating back in the $+x$ direction towards the stator with an amplitude of 94.4 dB. While there is an unknown level of transmission loss as this mode propagates through the stator, it will have a measurable impact on the amplitude and the phase of the scattered mode propagating in the $+x$ direction from the stator to the inlet, which has a predicted mode power level of 98.3 dB. An improved boundary treatment at the driver location is needed in order to reduce or eliminate these spurious reflections.

Table 4 compares the numerical predictions for transmission and reflection loss with the experimental data for transmission loss, as well as the magnitude of the energy in the scattered mode for the 14 vane stator. In all cases, the predicted acoustic transmission loss for the imposed azimuthal mode 6 is equal to the measured transmission loss, within the range of experimental error. In the case of the scattered counter-rotating azimuthal mode 8, the predicted acoustic transmission shows the correct trends for the magnitude of

Table 4. Predicted and Measured Transmission and Reflection Losses (dB) for Modes $(\pm 6, 0)$ **at 960 Hz**

Case	Mode (m,n)	Transmission Loss 14 Vane (Pred/Exp)	Reflection Loss 14 Vane	Transmission Loss 28 Vane (Pred/Exp)	Reflection Loss 28 Vane
3	$(-6, 0)$	-2.9/-3.0	-19.4	-1.2/-0.4	-26.1
	$(+8, 0)$	-8.3/-9.5	-3.8		
4	$(+6, 0)$	-0.0/-0.4	-19.3	-0.1/-0.7	-26.7
	$(-8, 0)$	-26.3/-15.2	-23.8		

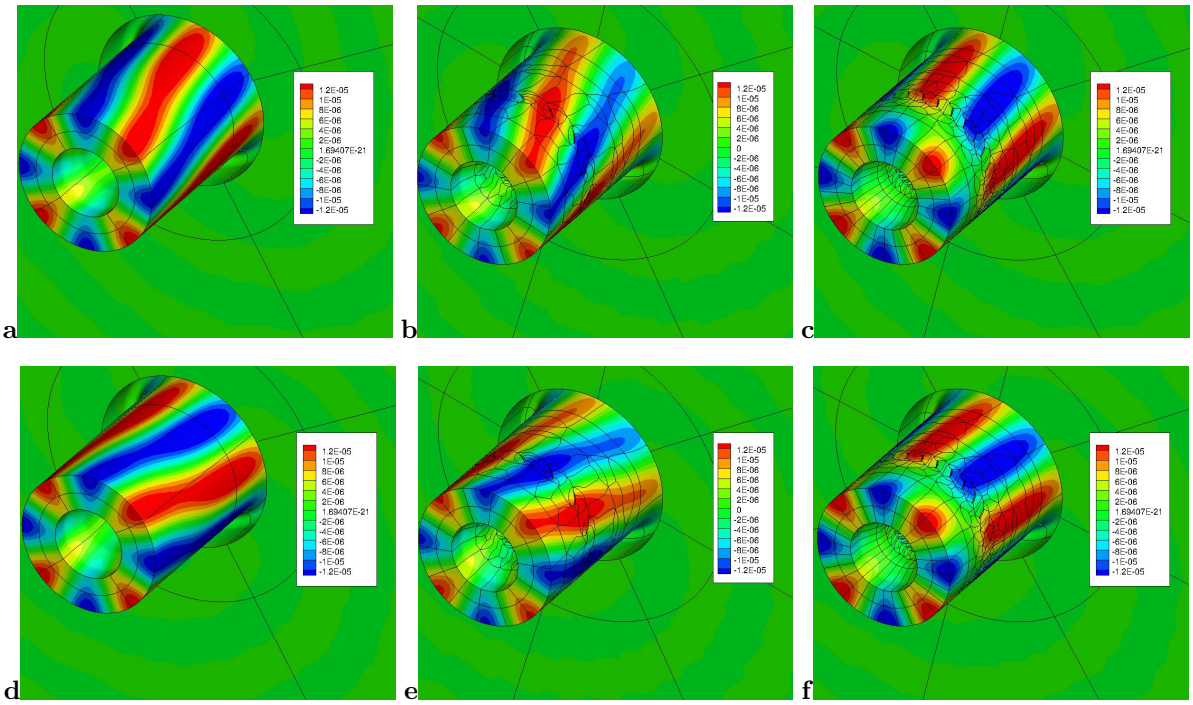

Figure 6. Predicted perturbation pressure contours at the start of a cycle for $(\pm 4, 0)$ mode at 480 Hz through the three ANCF configurations (a: $(-4, 0)$ clean, b: $(-4, 0)$ 14 vanes, c: $(-4, 0)$ 28 vanes d: $(+4, 0)$ clean, e: $(+4, 0)$ 14 vanes, f: $(+4, 0)$ 28 vanes)

the scattered mode, with reasonable agreement with experiment. This case highlights the need for improved boundary conditions.

E. Results for Modes $(\pm 4, 0)$ at 480 Hz

Figure 6 illustrates the propagation of the acoustic modes through the three geometries. The modes are very close to cut-off, and propagate at a very large angle to the x axis. As Figure 6 shows, the modes are nearly propagating in the azimuthal direction near the inlet. This test case highlights the errors in both the measurement and simulation of nearly cut-off modes.

As Table 2 shows, these modes reflect strongly from the inlet lip. This is expected behavior from nearly cut-off modes. However, the presence of strong modes propagating in both the positive and negative x directions results in large modeling errors from the experimental postprocessing. Thus, the predicted driver power level may have large errors. However, a newly-developed two-microphone rotating rake will allow the power levels of modes propagating in the positive and negative x directions to be determined, reducing or eliminating this source of error in future experiments.[32]

Table 5. Predicted and Measured Transmission and Reflection Losses (dB) for Modes $(\pm 4, 0)$ at 480 Hz

Case	Mode (m,n)	Transmission Loss 14 Vane (Pred/Exp)	Reflection Loss 14 Vane	Transmission Loss 28 Vane (Pred/Exp)	Reflection Loss 28 Vane
5	$(-4, 0)$	-2.1/-6.2	-23.3	-1.7/-11.0	-2.9
6	$(+4, 0)$	-2.1/-6.4	-23.3	-1.7/-11.1	-2.8

This case was also very demanding for the numerical simulations, due to the high mode power levels and very slow rate of propagation of the imposed modes. In addition, high levels of spurious reflection from the driver location boundary were seen.

Table 5 compares the numerical predictions for transmission and reflection with the experimental data for transmission. In these cases, the predicted acoustic transmission does not compare well with the experimental data. However, there are high levels of error in both the experimental and numerical data, making a meaningful comparison challenging until both the experimental postprocessing and numerical boundary conditions are improved.

VI. Conclusions

In this work, the NASA Computational Aeroacoustics code BASS was used to predict the transmission losses of acoustic modes propagating through a 3D stator. These predictions compared well with the experimentally measured data. While it must be emphasized that the cases considered did not include mean flow through the duct, the varying solidity and stagger angles of the stators made the test cases challenging.

The results of this study are verification of the ability of the BASS code to accurately predict the propagation, transmission, reflection, and scattering of acoustic modes in realistic geometries. With this verification completed, this work will continue moving towards the prediction of acoustic transmission for blade rows (both rotors and stators) in the presence of realistic mean flows.

Acknowledgments

This work is supported by the Fixed Wing Project of the NASA Fundamental Aeronautics Program.

References

[1]Tam, C.K.W., 'Computational Aeroacoustics: Issues and Methods', *AIAA Journal*, Vol. 33, No. 10, 1995, pp. 1788-96.

[2]Lele, S. K., 'Computational Aeroacoustics: A Review', AIAA Paper 97-0018, Jan. 1997.

[3]Tam, C.K.W., 'Computational Aeroacoustics: An Overview of Computational Challenges and Applications', *International Journal of Computational Fluid Dynamics*, Vol. 18, No. 6, 2004, pp. 547-567.

[4]Colonius, T. and Lele, S. K., 'Computational Aeroacoustics: Progress in Nonlinear Problems of Sound Generation', *Progress in Aerospace Sciences*, Vol. 40, No. 6, 2004, pp. 345-416.

[5]Mani, R., and Horvay, G., 'Sound Transmission Through Blade Rows',*J. Sound Vib.*, Vol. 12, No. 1, 1970, pp. 59-83.

[6]Smith, S. N., 'Discrete Frequency Sound Generation in Axial Flow Turbomachines', Aeronautical Research Council Reports and Memoranda No. 3709, HMSO, London, 1973.

[7]Hanson, D., 'Acoustic reflection and transmission of rotors and stators including mode and frequency scattering', AIAA Paper 1997-1610, May 1997.

[8]Hixon, R., 'Comparison of Computational Aeroacoustics Prediction of Acoustic Transmission through a 2D Stator with Flat Plate Theory', AIAA Paper 2012-0836, January 2012.

[9]Hixon, R., 'Comparison of Computational Aeroacoustics Prediction of Acoustic Transmission through a Loaded 2D Rotor with Flat Plate Theory', AIAA Paper 2012-2286, June 2012.

[10]Sutliff, D. L., 'A Mode Propagation Database Suitable for Code Validation Utilizing the NASA Glenn Advanced Noise Control Fan and Artificial Sources', 2014 AIAA Science and Technology Forum, National Harbor, Maryland (to be published).

[11]Hixon, R., Nallasamy, N. and Sawyer. S., 'Parallelization Strategy for an Explicit Computational Aeroacoustics Code', AIAA Paper 2002-2583, 2002.

[12]Nallasamy, M., Hixon, R., and Sawyer, S., 'Solution of unsteady Euler equations: Gust-cascade interaction tones', *Computers and Fluids*, Vol. 36, 2007, pp. 724-741.

[13]Hixon, R., Nallasamy, M., and Sawyer, S., 'Progress towards the prediction of turbomachinery noise using Computational Aeroacoustics', Inter-Noise paper IN06-119, Dec. 2006.

[14]Hixon, R., Golubev, V. V., Mankbadi, R. R., Scott, J. R., Sawyer, S., and Nallasamy, M., 'Application of a Nonlinear Computational Aeroacoustics Code to the Gust-Airfoil Problem', *AIAA Journal*, Vol. 44, 2006, pp. 323-328.

[15]Hixon, R., Nallasamy, M., Sawyer, S., and Dyson, R., 'Comparison of Numerical Schemes for a Realistic Computational Aeroacoustics Problem', *International Journal of Aeroacoustics*, Vol. 3, 2004, pp. 379-397.

[16]Sawyer, S., Nallasamy, M., Hixon, R., and Dyson, R. W., 'A Computational Aeroacoustic Prediction of Discrete-Frequency Rotor-Stator Interaction Noise: A Linear Theory Analysis', *International Journal of Aeroacoutics*, Vol. 3, No. 1, 2004, pp. 67-86.

[17]Snir, M., Otto, S., Huss-Lederman, S., Walker, D. and Dongarra, J., *MPI - The Complete Reference*, The MIT Press, Cambridge, Massachusetts, 1998.

[18]Allampali, V., Hixon, R., Nallasamy, M., and Sawyer, S., 'High-Accuracy Large-Step Explicit Runge-Kutta (HALE-RK) Schemes for Computational Aeroacoustics', *Journal of Computational Physics*, Vol. 228, No. 10, 2009, pp. 3837-3850.

[19]Hixon, R., Bhate, D., Nallasamy, M., and Sawyer, S., 'Shock-Capturing Dissipation Schemes for Computational Aeroacoustics', AIAA Paper 2006-2413, May 2006.

[20]Kennedy, C.A., Carpenter, M.H., 'Several New Numerical Methods for Compressible Shear-Layer Simulations', *Appl. Num. Math.*,Vol. 14, 1994, pp. 397-433.

[21]Tam, C. K. W., and Webb, J. C., 'Dispersion-Relation-Preserving Finite Difference Schemes for Computational Aeroacoustics', *J. of Comp. Phys.*, Vol. 107, No. 2, 1993, pp. 262-281.

[22]Envia, E., 'A High Frequency Model of Cascade Noise', AIAA Paper 1998-2318, June 1998.

[23]Giles, M., 'Nonreflecting Boundary Conditions for Euler Equation Calculations', *AIAA J.*, Vol. 28, 1990, pp. 2050-8.

[24]Loew, R.A., Lauer, J.T., MCAllister, J., and Sutliff, D.L., 'The Advanced Noise Control Fan', NASA TM-2006-214368, also AIAA-2006-3150, Nov 2006.

[25]McAllister, J., Loew, R.A., Lauer, J.T., and Sutliff, D.L., 'The Advanced Noise Control Fan Baseline Measurements', NASA TM-2009-215595, also AIAA-2009-0624, Oct 2009.

[26]Heidelberg, L.J., Hall, D.G., Bridges, J.E., and Nallasamy, N., 'A Unique Ducted Fan Test Bed for Active Noise Control and Aeroacoustics Research', NASA TM-107213, also AIAA-96-1740.

[27]Sutliff, D.L., Nallasamy, N., and Elliott, D.M., 'Baseline Acoustic Levels of the NASA Active Noise Control Fan Rig', NASA TM-107214, also AIAA-96-107214.

[28]Sutliff, D. L., 'Turbofan duct mode measurements using a continuously rotating microphone rake', *International Journal of Aeroacoustics*, Vol. 6, No. 2, April 2007, pp. 147-170.

[29]GridPro/az3000, Program Development Company, White Plains, NY, 1993-2010.

[30]Melville, R., 'Dynamic Aeroelastic Simulation of Complex Configurations Using Overset Grid Systems', AIAA 2000-2341, June 2000.

[31]Dahl, M. D. and Sutliff, D. L., 'Numerical Technique for Analyzing Rotating Rake Mode Measurements in a Duct with Passive Treatment and Shear Flow', AIAA Paper 2007-3679, 2007.

[32]Dahl, M. D., Hixon, R., and Sutliff, D. L., 'Further Development of Rotating Rake Mode Measurement Data Analysis', NASA TM-2013-217890, also AIAA 2013-2246, June 2013.

[33]Tyler , J. M., Sofrin, T. G., 'Axial flow compressor noise studies', *Transactions of the Society of Automotive Engineers*, Vol. 70, 1962, pp. 309-322.

Appendix I: Description of Incoming Acoustic Modes

The analysis presented here sketches that given by Envia,[22] and extends it to obtain the density and velocity perturbations associated with the incoming modes, which are required for the CAA analysis. This development is purposely left in dimensional form, to ensure that the flow variables can be easily nondimensionalized for use in the CAA code.

In this development, it is assumed that the flow perturbations associated with the acoustic modes introduced at the inflow boundary are low amplitude and is thus governed by the polar coordinate linearized Euler equations for a uniform axial mean flow:

$$\begin{aligned}
\rho_t + \overline{U}\rho_x + \overline{\rho}\left(\frac{v_r}{r} + (v_r)_r + \frac{1}{r}(v_\theta)_\theta + u_x\right) &= 0 \\
u_t + \overline{U}u_x + \frac{1}{\overline{\rho}}p_x &= 0 \\
(v_r)_t + \overline{U}(v_r)_x + \frac{1}{\overline{\rho}}p_r &= 0 \\
(v_\theta)_t + \overline{U}(v_\theta)_x + \frac{1}{\overline{\rho} r}p_\theta &= 0 \\
p_t + \overline{U}p_x + \gamma\overline{p}\left(\frac{v_r}{r} + (v_r)_r + \frac{1}{r}(v_\theta)_\theta + u_x\right) &= 0
\end{aligned} \tag{1}$$

These equations can be rearranged to obtain the convective wave equation:

$$p_{tt} + 2\overline{U}p_{xt} + \overline{U}^2 p_{xx} - \overline{a}^2\left(\frac{1}{r}p_r + p_{rr} + \frac{1}{r^2}p_{\theta\theta} + p_{xx}\right) = 0 \tag{2}$$

The perturbation pressure is assumed to be simple harmonic in time and in the azimuthal direction, and the product of the axial and radial functions:

$$p(x, r, \theta, t) = A_p f_m(r) g_m(x) e^{i(m\theta - \omega t)} \tag{3}$$

Substituting in, the convective wave equation becomes:

$$\begin{pmatrix} \left(\left(\overline{U}^2 - \overline{a}^2\right)\frac{d^2 g_m}{dx^2} - 2i\omega\overline{U}\frac{dg_m}{dx} - \omega^2 g_m\right) f_m \\ -\overline{a}^2\left(\frac{d^2 f_m}{dr^2} + \frac{1}{r}\frac{df_m}{dr} - \frac{m^2}{r^2} f_m\right) g_m \end{pmatrix} A_p e^{i(m\theta-\omega t)} = 0 \quad (4)$$

A separation constant κ^2 is introduced:

$$\begin{pmatrix} \left(\left(\overline{U}^2 - \overline{a}^2\right)\frac{d^2 g_m}{dx^2} - 2i\omega\overline{U}\frac{dg_m}{dx} - \left(\omega^2 - \overline{a}^2\kappa^2\right) g_m\right) f_m \\ -\overline{a}^2\left(\frac{d^2 f_m}{dr^2} + \frac{1}{r}\frac{df_m}{dr} + \left(\kappa^2 - \frac{m^2}{r^2}\right) f_m\right) g_m \end{pmatrix} A_p e^{i(m\theta-\omega t)} = 0 \quad (5)$$

and the equation simplifies to:

$$\begin{pmatrix} \left(\left(1 - M^2\right)\frac{d^2 g_m}{dx^2} + 2iM\frac{\omega}{\overline{a}}\frac{dg_m}{dx} + \left(\left(\frac{\omega}{\overline{a}}\right)^2 - \kappa^2\right) g_m\right) f_m \\ + \left(\frac{d^2 f_m}{dr^2} + \frac{1}{r}\frac{df_m}{dr} + \left(\kappa^2 - \frac{m^2}{r^2}\right) f_m\right) g_m \end{pmatrix} A_p e^{i(m\theta-\omega t)} = 0 \quad (6)$$

where $M = \frac{\overline{U}}{\overline{a}}$ is the Mach number.
Defining:

$$f_m(r) = f_{mn}(\kappa r) \quad (7)$$

gives:

$$\frac{d^2 f_m}{dr^2} + \frac{1}{r}\frac{df_m}{dr} + \left(\kappa^2 - \frac{m^2}{r^2}\right) f_m = \kappa^2\frac{d^2 f_{mn}}{d(\kappa r)^2} + \frac{\kappa}{r}\frac{df_{mn}}{d(\kappa r)} + \left(\kappa^2 - \frac{m^2}{r^2}\right) f_{mn} \quad (8)$$

Setting this equal to zero gives Bessel's equation:

$$(\kappa r)^2\frac{d^2 f_{mn}}{d(\kappa r)^2} + (\kappa r)\frac{df_{mn}}{d(\kappa r)} + \left((\kappa r)^2 - m^2\right) f_{mn} = 0 \quad (9)$$

which has a solution of the form:

$$f_{mn}(\kappa r) = c_1 J_n(\kappa r) + c_2 Y_n(\kappa r) \quad (10)$$

where n denotes the radial mode given by the solution.

At the inner and outer walls, the radial derivative of f_{mn} is zero (which specifies no flow through the wall):

$$\begin{aligned} c_1 J_n'(\kappa r_{hub}) + c_2 Y_n'(\kappa r_{hub}) &= 0 \\ c_1 J_n'(\kappa r_{tip}) + c_2 Y_n'(\kappa r_{tip}) &= 0 \end{aligned} \quad (11)$$

which gives the eigenvalue equation for radial mode n that the separation constant must satisfy as:

$$J_n'(\kappa_{mn} r_{tip}) Y_n'(\kappa_{mn} r_{hub}) - J_n'(\kappa_{mn} r_{hub}) Y_n'(\kappa_{mn} r_{tip}) = 0 \quad (12)$$

Here, κ_{mn} is the separation constant that satisfies the eigenvalue equation for azimuthal mode m and radial mode n.

Combining the constants and applying the boundary conditions, the function f_{mn} is given by Bessel functions of the form:

$$f_{mn}\left(\kappa_{mn}r\right) = C_{mn}\left(J_{mn}\left(\kappa_{mn}r\right) - \left(\frac{J'_{mn}\left(\kappa_{mn}r_{hub}\right)}{Y'_{mn}\left(\kappa_{mn}r_{hub}\right)}\right)Y_{mn}\left(\kappa_{mn}r\right)\right) \tag{13}$$

The function g_{mn} is given by:

$$g_{mn}\left(x\right) = e^{ik_{mn}x} \tag{14}$$

where the axial wavenumber k_{mn} satisfies the equation:

$$\left(1-M^2\right)k_{mn}^2 + 2k_{mn}M\frac{\omega}{\overline{a}} + \left(\kappa_{mn}^2 - \left(\frac{\omega}{\overline{a}}\right)^2\right) = 0 \tag{15}$$

which has the upstream and downstream running solutions:

$$k_{mn} = \left(\frac{1}{1-M^2}\right)\left(-\frac{M\omega}{\overline{a}} \pm \sqrt{\frac{\omega^2}{\overline{a}^2} - \left(1-M^2\right)\kappa_{mn}^2}\right) \tag{16}$$

At this point, the perturbation variables can be written as:

$$\begin{aligned}
p &= A_p f_{mn}\left(\kappa_{mn}r\right)e^{i(m\theta+k_{mn}x-\omega t)} \\
\rho &= A_p\left(\frac{1}{\overline{a}^2}\right)f_{mn}\left(\kappa_{mn}r\right)e^{i(m\theta+k_{mn}x-\omega t)} \\
u &= A_p\left(\frac{k_{mn}}{\overline{\rho}\left(\omega-k_{mn}\overline{U}\right)}\right)f_{mn}\left(\kappa_{mn}r\right)e^{i(m\theta+k_{mn}x-\omega t)} \\
v_r &= A_p\left(\frac{-i\kappa_{mn}}{\overline{\rho}\left(\omega-k_{mn}\overline{U}\right)}\right)f'_{mn}\left(\kappa_{mn}r\right)e^{i(m\theta+k_{mn}x-\omega t)} \\
v_\theta &= A_p\left(\frac{m}{\overline{\rho}\left(\omega-k_{mn}\overline{U}\right)r}\right)f_{mn}\left(\kappa_{mn}r\right)e^{i(m\theta+k_{mn}x-\omega t)}
\end{aligned} \tag{17}$$

These perturbation variables are imposed as an incoming wave at the boundary of the computational domain.

Note that the radial distribution of the perturbation pressure is identical for both upstream and downstream running acoustic modes.